XRISM spectroscopy on orbital modulation of Fe Lyα lines in Cygnus X-3

D Miura, N Hell, H Nakajima, S Watanabe, T Hayashi, S Kitamoto, K Yamaoka, J Miller, K Okabe, I Maruzuka, K Koljonen, H Yamaguchi, M McCollough, R Ballhausen, T Kallman, T Enoto, S Yamada, T Hakamata, R Tomaru, H Odaka
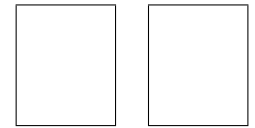
Lawrence Livermore National Laboratory

Disclaimer

This document was prepared as an account of work sponsored by an agency of the United States government. Neither the United States government nor Lawrence Livermore National Security, LLC, nor any of their employees makes any warranty, expressed or implied, or assumes any legal liability or responsibility for the accuracy, completeness, or usefulness of any information, apparatus, product, or process disclosed, or represents that its use would not infringe privately owned rights. Reference herein to any specific commercial product, process, or service by trade name, trademark, manufacturer, or otherwise does not necessarily constitute or imply its endorsement, recommendation, or favoring by the United States government or Lawrence Livermore National Security, LLC. The views and opinions of authors expressed herein do not necessarily state or reflect those of the United States government or Lawrence Livermore National Security, LLC, and shall not be used for advertising or product endorsement purposes.

This work performed under the auspices of the U.S. Department of Energy by Lawrence Livermore National Laboratory under Contract DE-AC52-07NA27344.

XRISM spectroscopy on orbital modulation of Fe Lyα lines in Cygnus X-3

Daiki Miura[1,2,*], **Hiroya Yamaguchi**[2,1,3], **Ralf Ballhausen**[4,5,6], **Timothy Kallman**[5], **Teruaki Enoto**[7], **Shinya Yamada**[8], **Tomohiro Hakamata**[9], **Ryota Tomaru**[9], **Hirokazu Odaka**[9], **Natalie Hell**[10], **Hiroshi Nakajima**[11], **Shin Watanabe**[2], **Tasuku Hayashi**[8], **Shunji Kitamoto**[8], **Kazutaka Yamaoka**[12], **Jon M. Miller**[13], **Keigo Okabe**[3], **Itsuki Maruzuka**[3], **Karri Koljonen**[14] and **Mike McCollough**[15]

[1] Department of Physics, Graduate School of Science, The University of Tokyo, 7-3-1 Hongo, Bunkyo-ku, Tokyo 113-0033, Japan
[2] Institute of Space and Astronautical Science (ISAS), Japan Aerospace Exploration Agency (JAXA), 3-1-1 Yoshinodai, Chuo-ku, Sagamihara, Kanagawa 252-5210, Japan
[3] Department of Science and Engineering, Graduate School of Science and Engineering, Aoyama Gakuin University, 5-10-1, Fuchinobe, Sagamihara 252-5258, Japan
[4] University of Maryland College Park, Department of Astronomy, College Park, MD 20742, USA
[5] NASA Goddard Space Flight Center, 8800 Greenbelt Rd, Greenbelt, MD 20771, USA
[6] Center for Research and Exploration in Space Science and Technology, NASA / GSFC (CRESST II), Greenbelt, MD 20771, USA
[7] Department of Physics, Kyoto University, Kitashirakawa-Oiwake-cho, Sakyo-ku, Kyoto, 606-8502, Japan
[8] Department of Physics, Rikkyo University, Toshima-Ku, Tokyo, 171-8501, Japan
[9] Department of Earth and Space Science, Graduate School of Science, Osaka University, 1-1 Machikaneyama, Toyonaka, Osaka 560-0043, Japan
[10] Lawrence Livermore National Laboratory, 7000 East Avenue, Livermore, CA 94550, USA
[11] College of Science and Engineering, Kanto Gakuin University, 1-50-1 Mutsuura Higashi, Kanazawa-ku, Yokohama, Kanagawa 236-8501, Japan
[12] Institute for Space-Earth Environmental Research (ISEE), Nagoya University, Furo-cho, Chikusa-ku, Nagoya, Aichi 464-8601, Japan
[13] Department of Astronomy, University of Michigan, Ann Arbor, MI 48109, USA
[14] Department of Physics, Norwegian University of Science and Technology, NO-7491 Trondheim, Norway
[15] Harvard-Smithsonian Center for Astrophysics, 60 Garden Street, Cambridge, MA 02138, USA

*E-mail: dikmur0611@g.ecc.u-tokyo.ac.jp

ORCID: 0009-0009-0439-1866, 0000-0002-5092-6085, 0000-0002-1118-8470, 0000-0003-1244-3100, 0000-0003-4808-893X, 0000-0002-6797-2539, 0000-0003-3057-1536, 0000-0001-6988-3938, 0000-0003-0441-7404, 0000-0001-8948-7983, 0000-0003-3841-0980, 0009-0004-9550-3643, 0009-0000-8402-9211, 0000-0002-9677-1533, 0000-0002-8384-3374

Abstract

To understand physical processes such as mass transfer and binary evolution in X-ray binaries, the orbital parameters of the system are fundamental and crucial information. Cygnus X-3 is a high-mass X-ray binary composed of a compact object of unknown nature and a Wolf-Rayet star, which is of great interest in the context of wind-fed mass accretion and binary evolution. Here we present XRISM/Resolve high-resolution spectroscopy focusing on the Fe Lyα lines in its hypersoft state. We perform an orbital phase-resolved spectral analysis of the lines to study the orbital modulation of the emission and absorption lines. It is found that the emission lines reflect the orbital motion of the compact object whose estimated velocity amplitude is 430^{+150}_{-140} $\mathrm{km\,s^{-1}}$, while the absorption lines show a variation that can be interpreted as originating from the stellar wind. We discuss possible mass ranges for the binary components using the mass function with the estimated value of the velocity amplitude in this work, combined with the relation between the mass loss rate and the orbital period derivative and the empirical mass and mass loss rate relation for Galactic Wolf-Rayet stars. They are constrained to be $(1.3$–$5.1)\,M_\odot$ and $(9.3$–$12)\,M_\odot$ for the assumed inclination angle of $i = 25°$, which becomes more relaxed to $(1.3$–$24)\,M_\odot$ and $(9.3$–$16)\,M_\odot$ for $i = 35°$, respectively. Thus, it remains unclear whether the system harbors a black hole or a neutron star.

Keywords: stars: individual (Cygnus X-3) — accretion, accretion disks — stars: Wolf–Rayet — stars: winds, outflows — X-rays: binaries

1 Introduction

Cygnus X-3 (hereafter Cyg X-3) is a unique Galactic high-mass X-ray binary consisting of a compact object and a WN4-6 type Wolf-Rayet (WR) companion star (Van Kerkwijk et al. 1992; van Kerkwijk 1993; van Kerkwijk et al. 1996; Koljonen & Maccarone 2017), located 9.7 ± 0.5 kpc from Earth (Reid & Miller-Jones 2023). WR stars have strong stellar winds, making them suitable targets for studying wind accretion. Since there are only two observed Galactic WR X-ray binaries – Cyg X-3 and OAO 1657-415 (Mason et al. 2009) – this system is a valuable target for observational studies of such a system. Indeed, many of the characteristics

observed in the X-ray spectra of Cyg X-3 are thought to originate from the strong stellar wind of the WR star (e.g., Kallman et al. 2019). The X-ray spectra display distinct signatures of the photoionized plasma, including emission lines, absorption lines, and narrow radiative recombination continua (RRCs) from highly ionized species of elements such as Si, S, and Fe (e.g., Kawashima & Kitamoto 1996; Paerels et al. 2000). The observation with XRISM, equipped with the microcalorimeter Resolve, has significantly enhanced the amount of information imprinted on the X-ray spectra regarding the photoionized plasma (XRISM Collaboration 2024).

WR X-ray binaries are expected to evolve into double compact binaries, which are gravitational wave sources, making their binary interactions a subject of great interest (e.g., Marchant & Bodensteiner 2024). The fate of Cyg X-3 was discussed in Belczynski et al. (2013), arguing that the system is a very likely double black hole or black-hole–neutron-star progenitor. In the study of binary evolution and the fundamental understanding of the system itself, orbital parameters represent the most basic and essential information. The orbital period of Cyg X-3 is well known to be $\sim 4.8\,$h. The orbital inclination of the system has been estimated using several different methods, which consistently yield a value of $\sim 30°$ (Vilhu et al. 2009, photoionized wind modeling; Antokhin et al. 2022, X-ray & IR photometry; Veledina et al. 2024a, Veledina et al. 2024b, X-ray polarimetry). Miller-Jones et al. (2004) also derived an orbital inclination of $\approx 30°$ from the proper motion analysis of the radio jets, whereas the precession modeling suggests a smaller inclination of $\lesssim 14°$. On the other hand, the masses of the compact object and WR star are not well determined, leaving it unclear whether the compact object is a black hole or a neutron star.

A commonly used method for estimating the masses of stars in a binary system is to measure the orbital velocity from the Doppler modulation of emission lines and derive the mass function. There have been several studies measuring the orbital velocity of the compact object in Cyg X-3. Vilhu et al. (2009) analyzed Chandra/HETG observational data and investigated the Doppler modulation of Fe Lyα emission lines. The Lyα emission in the photoionized plasma predominantly originates from cascade processes after the recombination between bare Fe nuclei and free electrons, which takes place in the regions closest to the compact object. Therefore, these lines serve as a probe of the motion of the compact object (although the degree of ionization also depends on the electron density). Based on this idea, Vilhu et al. (2009) measured the velocity amplitude of its circular motion to be $418 \pm 123\,\mathrm{km\,s^{-1}}$. However, this measurement is based on a modeling that does not account for the absorption lines detected by the Resolve (XRISM Collaboration 2024), as they could not be resolved with the spectral resolution of HETG. On the other hand, XRISM Collaboration (2024) conducted an orbital phase-resolved spectral analysis of the Fe K band using photoionized plasma modeling and estimated the orbital velocity of the compact object to be $194 \pm 29\,\mathrm{km\,s^{-1}}$ based on the Doppler shift of the emission line components. It is worth noting that the velocity amplitude of $\sim 200\,\mathrm{km\,s^{-1}}$ strongly supports the presence of a black hole in this system, as a lower velocity is expected for a more massive compact object. In that analysis, however, an assumption was made that all emission line components with different ionization states share a common velocity, and thus the velocity primarily determined by Fe Heα, not Fe Lyα, because of the higher photon statistics in the former. Since a more highly ionized plasma is expected to be formed closer to and probably confined by the compact object, it

is ideal to use the energy shift of the Fe Lyα lines for the velocity measurement.

In this paper, we focus exclusively on the Fe Lyα spectra observed with XRISM/Resolve and perform the measurement of the radial velocity of the compact object in Cyg X-3 by using a model that accounts for the presence of absorption lines. Details of the observation and data reduction are described in Section 2. The analysis and results are presented in Section 3, followed by a discussion of their implications in Section 4. Finally, we conclude this study in Section 5.

2 Observation and Data Reduction

The XRISM observation of Cyg X-3 was conducted as one of the Performance Verification (PV) observations, starting at 06:53:50 UT on 2024 March 24 until 15:37:46 UT on 2024 March 25 when the source was in a "hypersoft" state (ObsID: 300065010). To reduce the data, we followed the procedures described in the XRISM Quick-Start Guide ver. 2.3 using tools in HEAsoft ver. 6.34 and the calibration database (CALDB) ver. 8 (v20240815). The effective exposure after the screening was $\approx 67\,\mathrm{ks}$. The spectrum was extracted from High primary (Hp) grade events from all pixels except pixel 27 due to known calibration uncertainties. Large (L-type) Redistribution Matrix Files (RMFs) are created with the `rslmkrmf` task using the cleaned event file. Auxiliary Response Files (ARFs) are generated with the `xaarfgen` task.

3 Analysis and Results

To perform phase-resolved spectroscopy, we divide the orbital period into eight phase bins with equal width (i.e., 0.125 for each bin) by adopting the quadratic ephemeris of Antokhin & Cherepashchuk (2019) with an orbital period of $17\,252\,\mathrm{s}$ and extract spectra from each bin. Certain phases are always subject to visibility constraints due to the orbital period of Cyg X-3 being a multiple of the period over which XRISM orbits the Earth, and therefore phase $\varphi = 0.250$–0.375 is severely underexposed and unsuitable for spectral analysis.

The Fe Lyα spectra from the seven different phases are shown in Figure 1. These spectra show that the Fe Lyα profile is formed by the emission and absorption lines overlapping with each other. This overlap leads to parameter distributions with some local extrema, making it difficult to find the optimal solution using conventional optimization methods such as maximum likelihood estimation with C-statistics. Therefore, due to its flexibility, we adopt Bayesian inference based on the Markov Chain Monte Carlo (MCMC) method in the subsequent analysis.

3.1 Analyzing each phase independently

As a first step, we analyze the 6.8–7.1 keV spectrum extracted from each phase independently. The continuum component is modeled with a power law whose free parameters are the normalization K ($\mathrm{photons\,s^{-1}\,cm^{-2}\,keV^{-1}}$ at $1\,\mathrm{keV}$) and the photon index α. The emission and absorption lines are modeled with four Gaussian functions. Two of them correspond to the Lyα_1 and Lyα_2 emission, and the other two correspond to the Lyα_1 and Lyα_2 absorption. We fix the Lyα_1 and Lyα_2 line energies to their rest-frame values ($6.973\,\mathrm{keV}$ and $6.952\,\mathrm{keV}$, respectively) and set redshift z as free parameters. We also fix the Lyα_1/Lyα_2 flux ratios of both emission and absorption lines to 2. Removing this
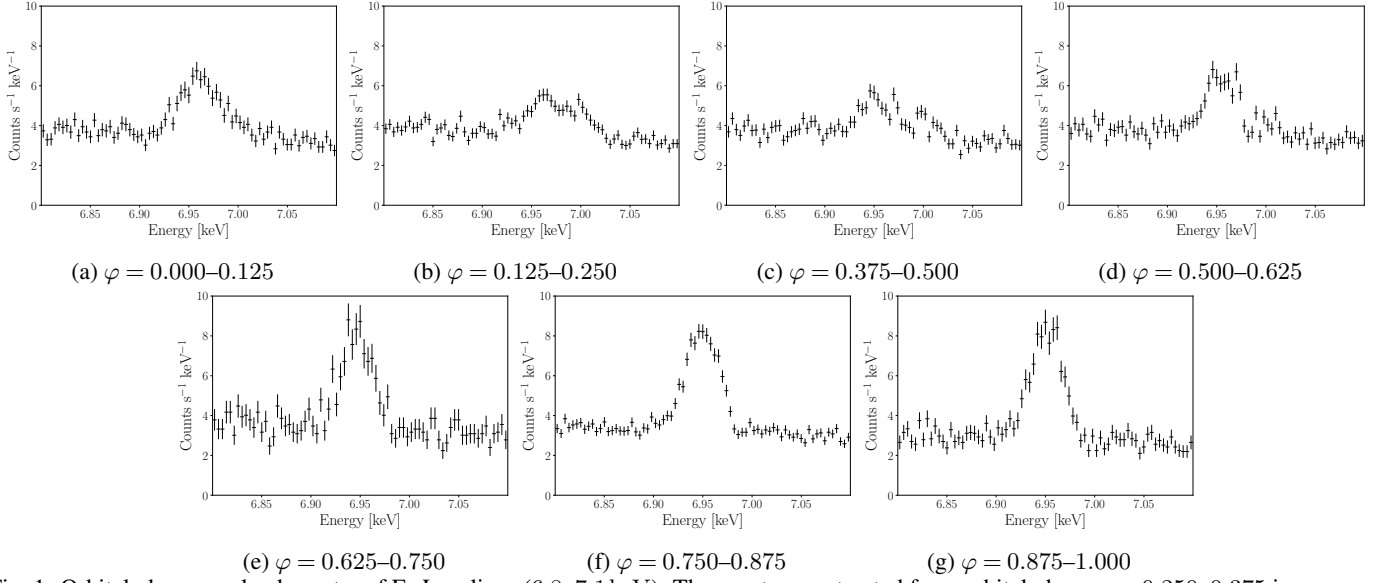
Fig. 1: Orbital phase-resolved spectra of Fe Lyα lines (6.8–7.1 keV). The spectrum extracted from orbital phase $\varphi = 0.250$–0.375 is removed because of severe underexposure due to the visibility constraint. The spectra are rebinned into 4 eV bins for clarity, although the unbinned spectra are used for the analysis.

assumption does not significantly affect the subsequent results or discussion. The redshift and width of the Lyα_1 and Lyα_2 lines are assumed to be identical within the emission or absorption component, but are treated independently between the emission and absorption. In summary, the free parameters of emission and absorption components are the redshift of emission and absorption lines (z_e and z_a), line width (σ_e and σ_a) and the normalization of the Lyα_2 line (N_e and N_a).

To optimize prior distributions for the parameters given above, we conduct an ad hoc spectral fitting based on C-statistic (Cash 1979) in XSPEC (Arnaud 1996). Only in this step, we fit the seven spectra simultaneously, assuming the common power-law normalization K and photon index α across the phases (i.e., in the subsequent MCMC analysis, these parameters are independent among the phases). The prior distributions optimized with this approach are summarized in Table 1. The parameters of the continuum component are sampled from a normal distribution with the mean values from this optimization and a standard deviation of 1. The line parameters are sampled from a uniform distribution over a range such that all values obtained by the optimization for each phase are included.

We then perform a Hamiltonian Monte Carlo (HMC; e.g., Neal 2011) No-U-Turn Sampler (NUTS; Hoffman & Gelman 2014) implemented in NumPyro (Phan et al. 2019), with 1000 warm-up steps for the adoption phase of HMC and 2000 samples. We set the maximum number of leapfrog steps at each iteration to be 1023. We use the Gelman-Rubin diagnostic (Gelman & Rubin 1992) to check convergence, and the condition $\hat{R} \leq 1.05$ for all parameters indicates that the MCMC chains have sufficiently converged.

The prediction (median) with the 90% highest probability density interval (HPDI) from the fitting for $\varphi = 0.375$–0.500 overlaid on the observed spectrum is shown in Figure 2. In Figure 9 in appendix 1, we also show those for all seven phases. The corner plot of posterior samples for $\varphi = 0.375$–0.500 is shown in Figure 3. There are some clear positive and negative correlations between the parameters. For example, as can be easily expected, the normalizations of emission and absorption lines (N_e and N_a) are an-

Table 1: Prior distributions of the model parameters.

Parameter	Prior distribution
Continuum	
Norm (K)	$\mathcal{N}(10.3, 1)^*$
Photon index (α)	$\mathcal{N}(2.75, 1)$
Emission lines	
Norm (N_e)	$\mathcal{U}(0, 5 \times 10^{-3})^{**}$
Width (σ_e) [keV]	$\mathcal{U}(5 \times 10^{-3}, 3 \times 10^{-2})$
Redshift (z_e)	$\mathcal{U}(-2 \times 10^{-3}, 3 \times 10^{-3})$
Absorption lines	
Norm (N_a)	$\mathcal{U}(-2 \times 10^{-3}, 0)$
Width (σ_a) [keV]	$\mathcal{U}(1 \times 10^{-3}, 3 \times 10^{-2})$
Redshift (z_a)	$\mathcal{U}(-2 \times 10^{-3}, 0)$

* $\mathcal{N}(\mu, \sigma)$ represents a normal distribution with a mean of μ and a standard deviation of σ.

** $\mathcal{U}(x_l, x_h)$ represents a uniform distribution in the range from x_l to x_h.

ticorrelated. The redshift of the emission lines z_e, which is of the most interest in this study, correlates with N_a and σ_e, but anticorrelates with N_e and σ_a.

Table 2 in appendix 1 provides the medians of the marginal posteriors and their 90% HPDIs. This table also presents the C-statistics with corresponding degrees of freedom (dof), calculated using the medians of the model predictions obtained through the HMC method, for the purpose of evaluating the model quality. We heve obtained acceptable C-statistic/dof values. Figure 4 shows the resulting velocity, flux, width, and equivalent width (EW) as a function of orbital phase for each of the emission and absorption lines, where $v = cz$ (c is the speed of light) is used to convert redshift to velocity. The velocity of the emission line component shows a significant orbital modulation, with the largest blueshift at around phase 0.25 and the largest redshift at around 0.75, indicating that the Fe Lyα emission lines originate from the vicinity of
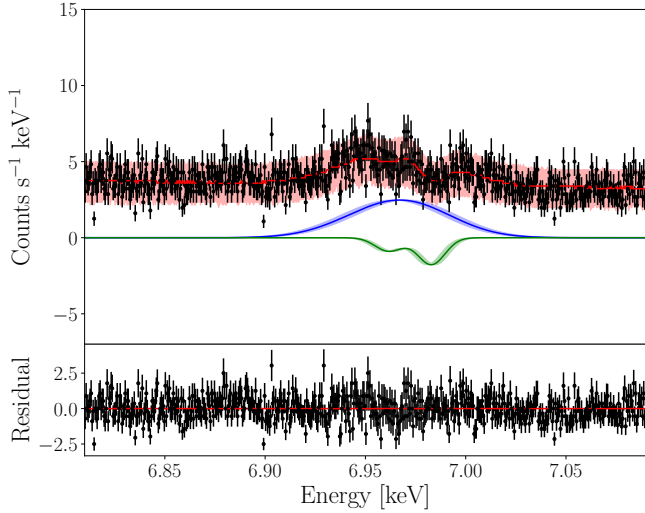
Fig. 2: Top: The prediction (median) with the 90% HPDI from the fitting for $\varphi = 0.375$–0.500 overlaid on the observed spectrum. The red solid line represents the predicted median spectrum and red-shaded region represents 90% HPDI. The blue and green solid lines show the emission and absorption lines with the medians of posterior samples of the parameters described in Table 2 in appendix 1. The blue- and green-shaded region correspond to the 90% HPDIs for redshifts (z_e and z_a). Bottom: The residual from the median.

the compact star, and the velocity shifts track the orbital motion of the compact star as expected.

3.2 Analyzing all the phases simultaneously assuming a circular orbit

As demonstrated in the previous section, the velocity shift of the emission lines indicates the orbital motion of the compact star. We therefore introduce more sophisticated approach, where the spectra of all the phases are analyzed simultaneously, assuming a circular motion for the velocity shift of the emission line component. Specifically, the redshift of the Gaussian is represented by the following equation:

$$z_e = \frac{v_0}{c} - \frac{v}{c} \sin\{2\pi(\varphi + \varphi_0)\} \quad (1)$$

where v_0, v, φ and φ_0 are the velocity offset, the velocity amplitude, the orbital phase, and the phase offset, respectively. Antokhin & Cherepashchuk (2019) investigated the orbital period and its variation using observational data from multiple X-ray telescopes and detected a sinusoidal perturbation in the period. If this perturbation is interpreted as apsidal motion, the eccentricity of the orbit is estimated to be ≈ 0.03. Therefore, assuming a circular orbit should be reasonable.

Based on the assumption outlined above, the analysis is performed in the same manner as in the previous section. The priors for the velocity offset, the velocity amplitude, and the phase offset are sampled from a uniform distribution with the range of $[-100, 300]$ km s^{-1}, $[200, 700]$ km s^{-1}, $[-0.15, 0.15]$, respectively. For the other parameters, the priors are sampled using the same method as in the previous section. The orbital phase φ is fixed at the median of the phase range from which each spectrum is extracted for each bin. We perform an HMC-NUTS with 1000 warm-up steps and 2000 samples. All parameters satisfy the

condition $\hat{R} \leq 1.05$, which indicates sufficient convergence of the MCMC chains.

The predictions (median) with the 90% HPDIs from the fitting for all phases overlaid on the observed spectra are shown in Figure 10 in appendix 1. The corner plot of the posterior samples is also shown in Figure 5. Figure 6 shows the resulting parameters as a function of the orbital phase, while Table 3 in appendix 1 provides the medians of the marginal posteriors and their 90% HPDIs with the C-statistic and dof. We have obtained an acceptable value of C-statistic/dof value. The velocity amplitude, the velocity offset, and the phase offset are $v = 430^{+150}_{-140}$ km s^{-1}, $v_0 = 100^{+93}_{-110}$ km s^{-1}, and $\varphi_0 = -0.02^{+0.05}_{-0.04}$, respectively. The flux of the emission line seems to be minimum in orbital phase 0.5 and maximum in 0.0. The width of the emission line remains roughly constant, though it is slightly larger in $\varphi = 0.385$–0.500. The absorption lines are overall blueshifted by > 250 km s^{-1} and appear to show a small-amplitude modulation, with the blueshift being minimal around $\varphi = 0.0$ and maximal around $\varphi = 0.5$. The flux variation is not clear.

4 Discussion

4.1 Summary of the Results and Comparison with Previous Work

We have performed an orbital phase-resolved analysis of the X-ray spectra of Cyg X-3 in its hypersoft state obtained by XRISM. To measure the radial velocity of the compact star, we have conducted the analysis focusing on the Fe Lyα emission and absorption lines. By analyzing the spectra extracted from each phase independently, we have confirmed that, as expected, the velocity shift of the emission lines reflects the orbital motion of the compact object. We have proceeded with the analysis by assuming the velocity shift of the emission lines follows a sine curve, as described in Equation 1. As a result, the orbital velocity amplitude of the compact object is determined to be $v = 430^{+150}_{-140}$ km s^{-1}. The velocity offset includes 0 km s^{-1} within the 90% HPDI. These estimated values are consistent with those reported in Vilhu et al. (2009), though the absorption lines were not taken into account in their analysis due to the insufficient spectral resolution of Chandra/HETG.

XRISM Collaboration (2024) analyzed the same dataset as this study. As mentioned earlier, their analysis of the Fe K band spectra employed the model with three photoionized plasma components of different ionization degrees for both emission and absorption lines. The three emission components and the three absorption components were each constrained to share a common Doppler shift. As a result, the orbital velocity amplitude of the emission components was found to be 194 ± 29 km s^{-1}, significantly smaller than the values obtained in this study and by Vilhu et al. (2009). This was likely because the velocity was primarily determined by the less ionized component, which represents the complex spectral structure of the Fe Heα emission. Our result suggests that the most highly ionized plasma emitting Fe Lyα lines is spatially separated from the less ionized plasma responsible for the Fe Heα emission and exhibits distinct motion.

The same applies to the absorption lines, whose Doppler shift is primarily determined by the low-ionization component in XRISM Collaboration (2024). In the previous study, the velocity amplitude and offset of the absorption lines are reported as 55 ± 7 km s^{-1} and -534 ± 6 km s^{-1}, respectively. The phase at which the blueshift is maximum is $\varphi \sim 0.1$. In this study, however, the systemic velocity of the absorption line is found to be ~ -300 km s^{-1}, whose abso-
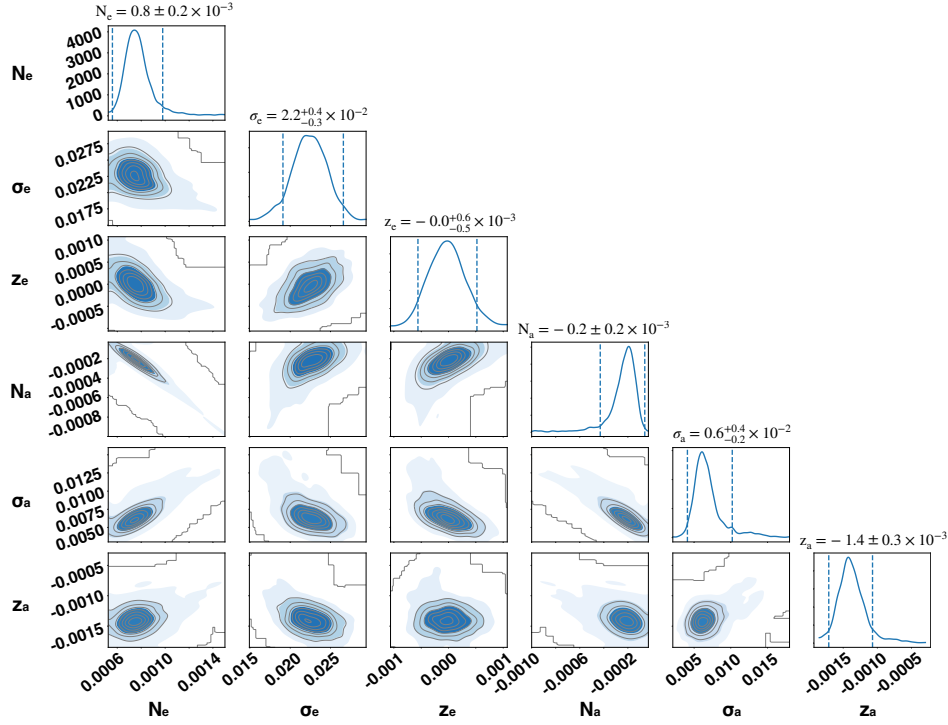
Fig. 3: Corner plot of the posterior samples from $\varphi = 0.375$–0.500 when analyzing each phase independently(subsection 3.1). The vertical dashed lines indicate the 90% HPDIs.
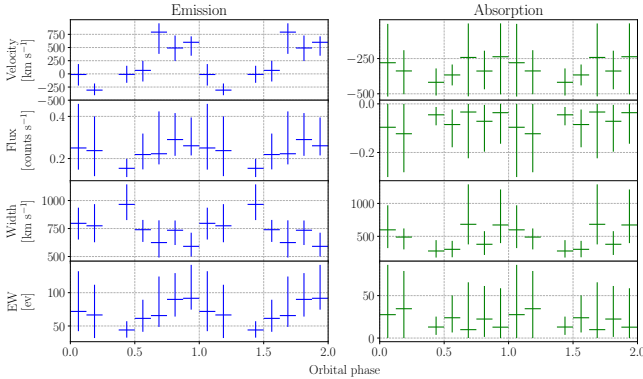

Fig. 4: Line parameters obtained for the emission (left) and absorption (right) components as a function of the orbital phase when analyzing each phase independently (subsection 3.1). From top to bottom, they represent the velocities, fluxes, widths, and equivalent widths (EWs).

lute value is smaller than the result from XRISM Collaboration (2024). The modulation pattern also differs, with the phase at which the maximum blueshift occurs being $\varphi \sim 0.5$ (Figure 6).

The absorption line width shows a slight orbital modulation with the maximum and minimum at $\varphi \sim 0.0$ and $\varphi \sim 0.5$, respectively, while the absorption line flux does not show a clear modulation (Figure 6). Based on the orbital variations of the absorption line parameters described above, it can be interpreted that the absorption lines are formed in the stellar wind of the donor WR star (Figure 7). At the inferior conjunction ($\varphi = 0.5$), the absolute value of the stellar wind line-of-sight velocity is maximized. At the superior conjunction ($\varphi = 0.0$), the observed line width is maximum because of the velocity gradient along the line of sight.

The smaller blueshift derived from the Lyα absorption lines in this work can also be naturally explained by the configuration illustrated in Figure 7; the higher the ionization (i.e., the closer to the compact object), the smaller the projected component along the line of sight. A careful investigation of various other absorption lines is an important future task for revealing the detailed velocity structure of the stellar wind.

4.2 Constraints on the System Masses

The orbital velocity amplitude of the compact object is related to the mass of the compact object M_C and the mass of the WR star M_{WR} through the mass function

$$\frac{P_{orb} K_C^3}{2\pi G} = \frac{M_{WR}^3 \sin^3 i}{M_{tot}^2} \quad (2)$$

where $P_{orb} = 17252\,\mathrm{s}$ is the orbital period, K_C is the velocity amplitude of the compact object, G is the gravitational constant, i is the inclination angle of the system, and $M_{tot} = M_C + M_{WR}$ is the total mass of the system. In the following discussion, we assume $i = 25°$–$35°$(Vilhu et al. 2009; Antokhin et al. 2022; Veledina et al. 2024a; Veledina et al. 2024b). In general, measurement of the velocity amplitude of the WR star K_{WR} with optical or infrared spectroscopy determines the masses of both compact object and WR star using another mass function

$$\frac{P_{orb} K_{WR}^3}{2\pi G} = \frac{M_C^3 \sin^3 i}{M_{tot}^2} \quad (3)$$

along with Equation 2. However, this method cannot be applied to this system. The position of Cyg X-3 in the Galactic plane leads to strong interstellar extinction, making it impossible to detect its optical/UV counterpart. Therefore, we cannot measure the velocity amplitude of the WR star with optical or UV spectroscopy. Infrared spectroscopy is available. Hanson et al. (2000)
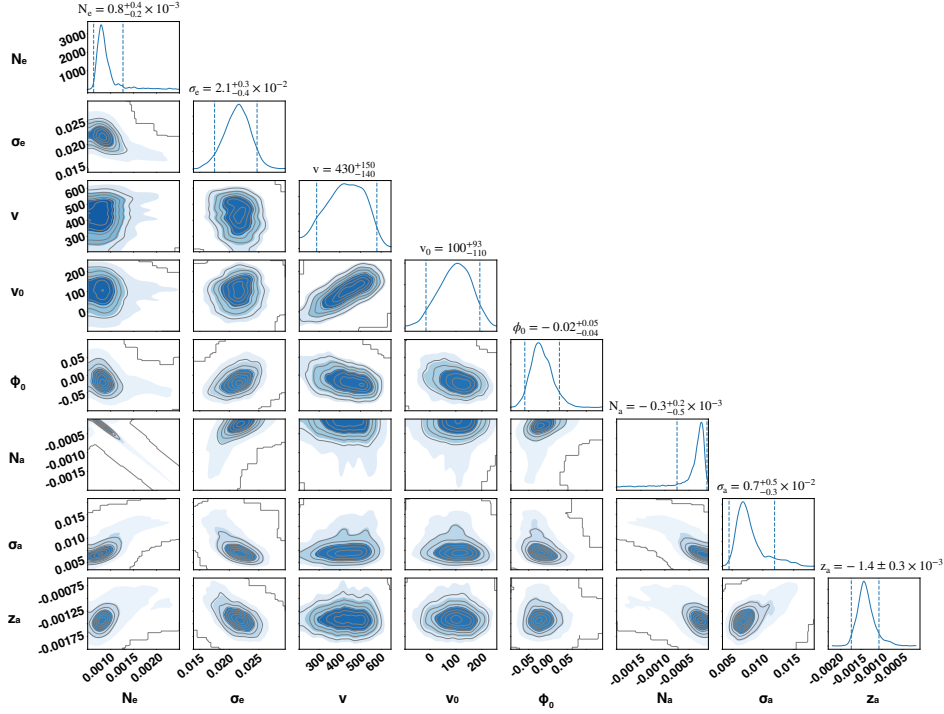
Fig. 5: The same figure as Figure 3 but obtained by the analysis assuming a circular orbit(subsection 3.2).
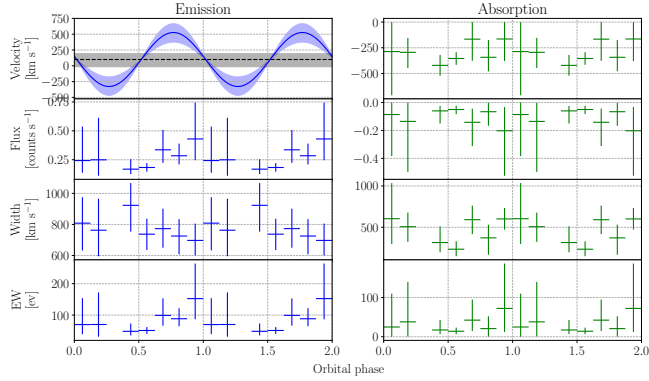

Fig. 6: The same figure as Figure 4 except for the velocity of the emission component (top-left panel), but obtained by the analysis assuming a circular orbit. The blue solid line represents the velocity curve of the emission component with the median of the posterior samples of the velocity amplitude, the velocity offset, and the phase offset. The blue-shaded region corresponds to the 90% HPDI of the velocity amplitude. The gray dashed line and the gray-shaded region represent the median and the 90% HPDI of the posterior samples of the velocity offset, respectively.
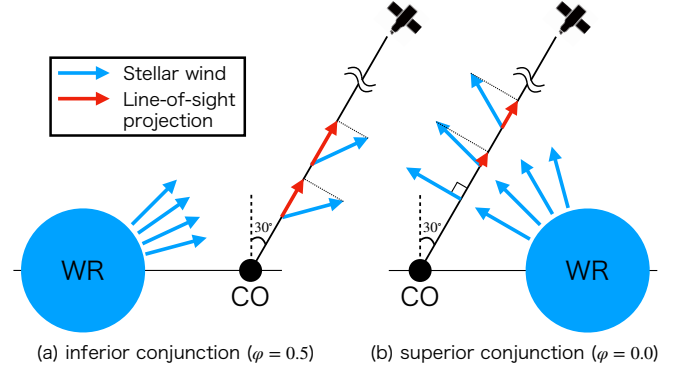

Fig. 7: Schematic illustration of the possible stellar wind structure of the WR star in Cyg X-3. (a) corresponds to the inferior conjunction ($\varphi = 0.5$), and (b) to the superior conjunction ($\varphi = 0.0$) configuration. The blue arrows represent the stellar wind velocity vectors, and the red arrows represent their line-of-sight projections.

indeed detected the He I 2p-2s $2.058\,\mu$m absorption line using the FSpec infrared spectrometer at Steward Observatory, which was then used to measure the velocity amplitude of the WR star. However, with Gemini/GNIRS infrared spectroscopy, Koljonen & Maccarone (2017) concluded that the absorption line is not due to the WR star but is formed by the stellar wind. This calls into question the reliability of the published mass function of Cyg X-3 (e.g., Zdziarski et al. 2013). Furthermore, they argued that the infrared emission lines are from a region larger than the binary orbit, making it difficult to determine the orbital parameters using

infrared spectroscopy. Note that the difference between the results of the two preceding studies is discussed in detail in Koljonen & Maccarone (2017).

Figure 8 shows planes where the horizontal and vertical axes represent the masses of the WR star and the compact object, respectively. By substituting the orbital velocity amplitude of the compact object obtained in this study $K_C = 430^{+150}_{-140}$ km s^{-1} into Equation 2, the masses of this system are constrained to the regions shown in red on these planes. The panel (a) shows the case with the assumed inclination angle $i = 25^\circ$, while the panel (b) shows the case with $i = 35^\circ$. The region shown in blue is obtained from the relation

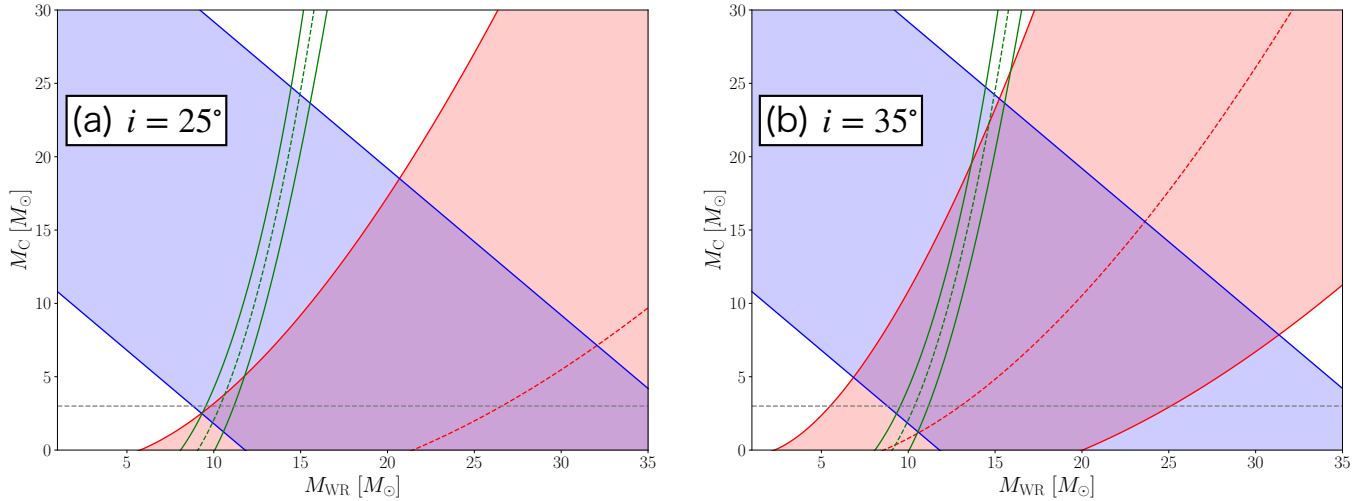$$\frac{2\dot{M}}{M_{\rm tot}} = \frac{\dot{P}}{P} \qquad (4)$$

Fig. 8: The allowed masses of the compact object and the WR star. The red regions are obtained from Equation 2 with the orbital velocity amplitude of the compact object obtained in this study, where panel (a) assumes an inclination angle of $i = 25°$ and panel (b) assumes $i = 35°$. The blue and green regions are obtained from Equations 4 and 6, respectively. The horizontal dashed lines represent $3\,M_\odot$, theoretically predicted as the upper mass limit of neutron stars.

where $\dot{M}$ is the mass loss rate of the system by the stellar wind of the WR star and $\dot{P}$ is the orbital period derivative. This relation is derived from the slowing down of the binary orbit due to the angular momentum loss, with the assumptions that the binary is detached, that any effects from tidal interaction can be ignored (e.g., Bagot 1996), and that the stellar wind removes almost all the specific angular momentum with only a small fraction being accreted onto the compact object. The value of $\dot{P}/P$ has been reported as $1.02 \times 10^{-6}\,\mathrm{yr}^{-1}$ (Antokhin & Cherepashchuk 2019). The mass loss rate is estimated in Koljonen & Maccarone (2017) to be $\dot{M} = (0.6 - 2.0) \times 10^{-5}\,M_\odot\,\mathrm{yr}^{-1}$ by WR atmospheric modeling of infrared spectra, assuming a wind clumping factor of $D = 3.3$–14.3 (Szostek & Zdziarski 2008) and a distance of $d = 10.2\,\mathrm{kpc}$. An additional constraint on the masses can be obtained from the empirical relation between the mass loss rates and the masses of Galactic WR stars of the WN type, which is given by Zdziarski et al. (2013) as

$$M_{\mathrm{WR}} = \langle M \rangle \left(\frac{\dot{M}}{\dot{M}_0} \right)^{1/n} \quad (5)$$

$$\dot{M}_0 = (1.9 \pm 0.2) \times 10^{-5}\,M_\odot\,\mathrm{yr}^{-1}, \quad n = 2.93 \pm 0.38$$

where $\langle M \rangle = 14.7\,M_\odot$ is the geometric average of the masses of WR star samples and $\dot{M}_0$ is the mass loss rate at $M_{\mathrm{WR}} = \langle M \rangle$. This relation is valid only for $M_{\mathrm{WR}} < 22\,M_\odot$. By eliminating $\dot{M}$ from Equation 4 and 5, we obtain

$$M_{\mathrm{C}} = \frac{2\dot{M}_0 P}{\langle M \rangle^n \dot{P}} M_{\mathrm{WR}}^n - M_{\mathrm{WR}} \quad (6)$$

which is shown in green in Figure 8. The masses of the compact object and the WR star are constrained to be $M_{\mathrm{C}} = (1.3$–$5.1)\,M_\odot$ and $M_{\mathrm{WR}} = (9.3$–$12)\,M_\odot$ for $i = 25°$, and $M_{\mathrm{C}} = (1.3$–$24)\,M_\odot$ and $M_{\mathrm{WR}} = (9.3$–$16)\,M_\odot$ for $i = 35°$, respectively. These WR star masses are consistent with that estimated in Koljonen & Maccarone (2017) from the theoretical mass-luminosity relation of WR stars (Gräfener et al. 2011). The estimated masses of the compact object here do not allow us to determine whether it is a neutron star or a black hole.

5 Conclusions

We have presented a high-resolution spectral analysis of the Fe Lyα emission and absorption lines of Cyg X-3 obtained by XRISM/Resolve when the system is in its hypersoft state. The spectra extracted from seven different orbital phase bins are well reproduced by a Doppler shift model of emission lines due to the circular motion of the compact object. Gaussian functions are used to represent the emission and absorption lines with a flexible MCMC method, enabling successful parameter estimation even in spectra where the emission and absorption lines overlap. The compact object is found to have a velocity amplitude of $K_{\mathrm{C}} = 430^{+150}_{-140}\,\mathrm{km\,s}^{-1}$. This value is significantly larger than that obtained by XRISM Collaboration (2024) which is primarily determined by the Fe Heα lines rather than the Fe Lyα lines, suggesting that the emitting regions of the two lines are spatially and kinematically separated. The absorption lines are naturally interpreted as reflecting the velocity structure of the stellar wind from the WR star. A systematic investigation of various other absorption lines is an important direction for future work, as it may shed light on the detailed velocity structure of the stellar wind.

Based on the result of the velocity amplitude of the compact object, we have discussed the mass of the compact object and the WR star. The mass function obtained by substituting the velocity amplitude derived in this study, combined with the relation between the mass loss rate and the orbital period derivative and the empirical relation of the mass loss rate and the mass of the Galactic WN type WR stars, allows us to constrain the mass of the compact object to be $M_{\mathrm{C}} = (1.3$–$5.1)\,M_\odot$ and $M_{\mathrm{WR}} = (9.3$–$12)\,M_\odot$ for the assumed orbital inclination angle of $i = 25°$, and $M_{\mathrm{C}} = (1.3$–$24)\,M_\odot$ and $M_{\mathrm{WR}} = (9.3$–$16)\,M_\odot$ for $i = 35°$, respectively. This means the identity of the compact object is still uncertain.

Appendix 1 Additional Spectral Fits and Parameters

Figure 9 shows the predictions (median) with the 90% HPDIs from the fitting for all seven phases overlaid on the observed spectra for the analysis of each phase independently. Table 2 provides the medians of the marginal posteriors and their 90% HPDIs with the C-statistic/dofs.

Figure 10 shows the predictions (median) with the 90% HPDIs from the fitting for all seven phases overlaid on the observed spectra for the analysis assuming a circular orbit. Table 3 provides the medians of the marginal posteriors and their 90% HPDIs with the C-statistic/dof.

References

Antokhin, I. I., & Cherepashchuk, A. M. 2019, The Astrophysical Journal, 871, 244,

Antokhin, I. I., Cherepashchuk, A. M., Antokhina, E. A., & Tatarnikov, A. M. 2022, The Astrophysical Journal, 926, 123,

Arnaud, K. A. 1996, in Astronomical Data Analysis Software and Systems V, Vol. 101, 17

Bagot, P. 1996, Astronomy and Astrophysics, 314, 576

Belczynski, K., Bulik, T., Mandel, I., et al. 2013, The Astrophysical Journal, 764, 96,

Cash, W. 1979, The Astrophysical Journal, 228, 939,

Gelman, A., & Rubin, D. B. 1992, Statistical Science, 7,

Gräfener, G., Vink, J. S., De Koter, A., & Langer, N. 2011, Astronomy & Astrophysics, 535, A56,

Hanson, M. M., Still, M. D., & Fender, R. P. 2000, The Astrophysical Journal, 541, 308,

Hoffman, M. D., & Gelman, A. 2014, Journal of Machine Learning Research, 15, 1593

Kallman, T., McCollough, M., Koljonen, K., et al. 2019, The Astrophysical Journal, 874, 51,

Kawashima, K., & Kitamoto, S. 1996, Publications of the Astronomical Society of Japan, 48, L113,

Koljonen, K. I. I., & Maccarone, T. J. 2017, Monthly Notices of the Royal Astronomical Society, 472, 2181,

Marchant, P., & Bodensteiner, J. 2024, Annual Review of Astronomy and Astrophysics, 62, 21,

Mason, A. B., Clark, J. S., Norton, A. J., Negueruela, I., & Roche, P. 2009, Astronomy & Astrophysics, 505, 281,

Miller-Jones, J. C. A., Blundell, K. M., Rupen, M. P., et al. 2004, The Astrophysical Journal, 600, 368,

Neal, R. M. 2011, in Handbook of Markov Chain Monte Carlo, 1st edn., ed. S. Brooks, A. Gelman, G. Jones, & X.-L. Meng (New York: Chapman and Hall/CRC),

Paerels, F., Cottam, J., Sako, M., et al. 2000, The Astrophysical Journal, 533, L135,

Phan, D., Pradhan, N., & Jankowiak, M. 2019, arXiv:1912.11554,

Reid, M. J., & Miller-Jones, J. C. A. 2023, The Astrophysical Journal, 959,

85,

Szostek, A., & Zdziarski, A. A. 2008, Monthly Notices of the Royal Astronomical Society, 386, 593,

van Kerkwijk, M. H. 1993, Astronomy and Astrophysics, 276, L9

van Kerkwijk, M. H., Geballe, T. R., King, D. L., van der Klis, M., & van Paradijs, J. 1996, Astronomy and Astrophysics, 314, 521,

Van Kerkwijk, M. H., Charles, P. A., Geballe, T. R., et al. 1992, Nature, 355, 703,

Veledina, A., Muleri, F., Poutanen, J., et al. 2024a, Nature Astronomy, 8, 1031,

Veledina, A., Poutanen, J., Bocharova, A., et al. 2024b, Astronomy & Astrophysics, 688, L27,

Vilhu, O., Hakala, P., Hannikainen, D. C., McCollough, M., & Koljonen, K. 2009, Astronomy & Astrophysics, 501, 679,

XRISM Collaboration. 2024, The Astrophysical Journal Letters, 977, L34,

Zdziarski, A. A., Mikołajewska, J., & Belczyński, K. 2013, Monthly Notices of the Royal Astronomical Society: Letters, 429, L104,
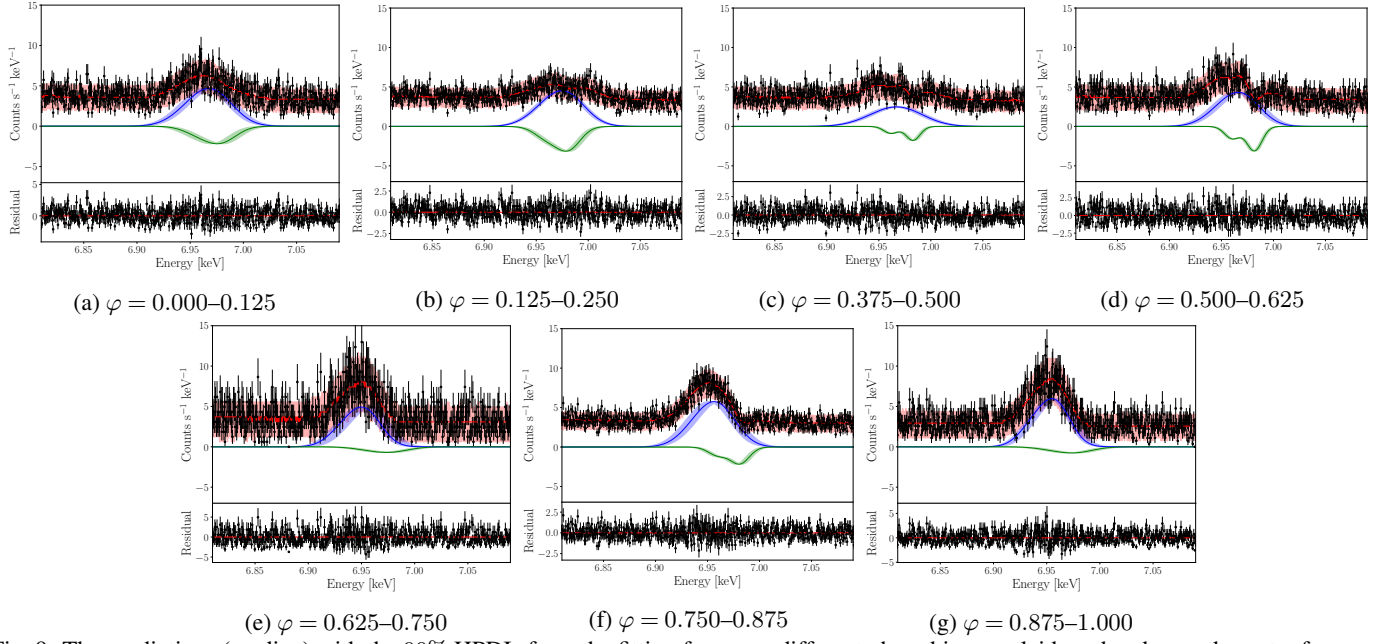
Fig. 9: The predictions (median) with the 90% HPDIs from the fitting for seven different phase bins overlaid on the observed spectra for the analysis of each phase independently(subsection 3.1). For each phase bin, the top panel shows the predicted median spectrum (red solid line) and the 90% HPDI (red-shaded region). The blue and green solid lines show the emission and absorption lines with the medians of posterior samples of the parameters described in Table 1. The blue- and green-shaded regions correspond to the 90% HPDIs for redshifts (z_e and z_a). The bottom panel shows the residual from the median.
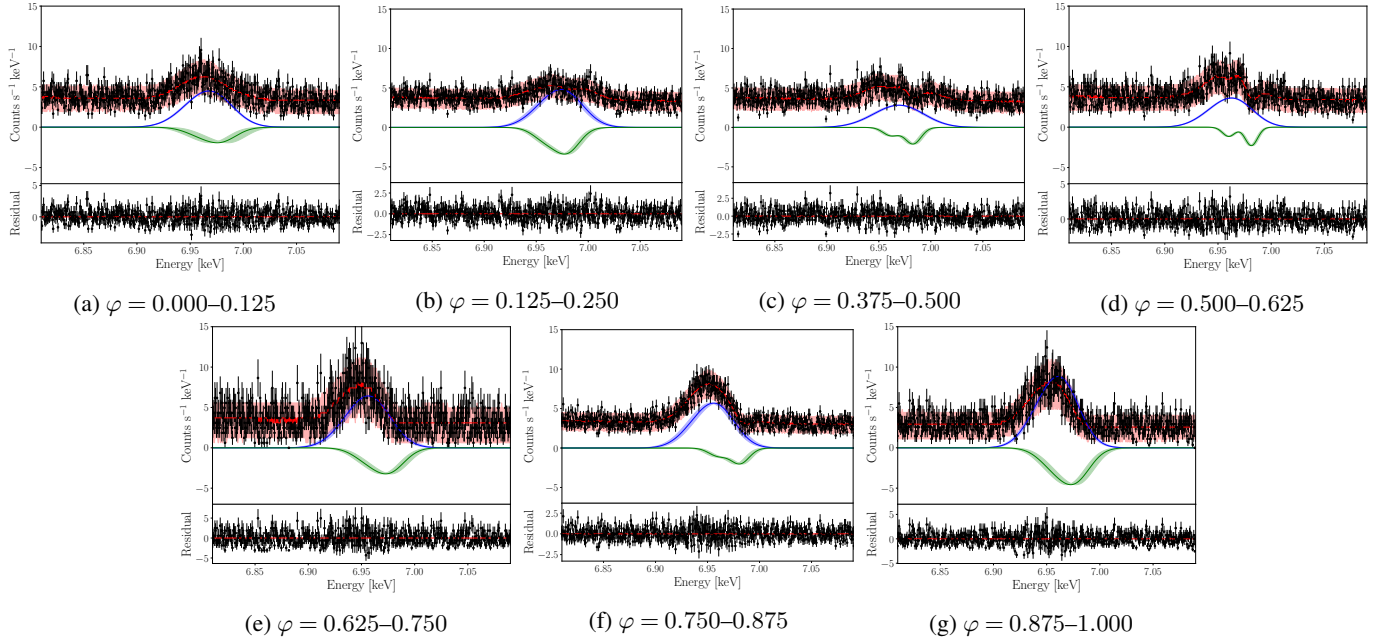

Fig. 10: The same figure as Figure 9 but obtained by the analysis assuming a circular orbit(subsection 3.2).

Table 2: Median and 90% interval of inferred parameters when analyzing each phase independently(subsection 3.1).

Parameter \ Phase*	$\varphi = 0.0625$	$\varphi = 0.1875$	$\varphi = 0.4375$	$\varphi = 0.5625$	$\varphi = 0.6875$	$\varphi = 0.8125$	$\varphi = 0.9375$
Continuum							
Flux ($10^{-9}\,\mathrm{erg\,cm^{-2}\,s^{-1}}$)**	$1.17^{+0.03}_{-0.02}$	1.19 ± 0.02	1.17 ± 0.02	$1.20^{+0.03}_{-0.02}$	1.12 ± 0.04	1.07 ± 0.02	0.94 ± 0.03
Photon index (α)	2.73 ± 0.08	$2.73^{+0.07}_{-0.09}$	2.73 ± 0.08	$2.72^{+0.08}_{-0.09}$	$2.76^{+0.08}_{-0.09}$	$2.77^{+0.09}_{-0.08}$	$2.83^{+0.08}_{-0.09}$
Emission lines							
Norm (N_e) $\times 10^{-3}$	$1.2^{+1.0}_{-0.5}$	$1.2^{+0.8}_{-0.6}$	0.8 ± 0.2	$1.1^{+0.5}_{-0.4}$	1.1 ± 0.2	$1.4^{+0.6}_{-0.4}$	$1.3^{+0.7}_{-0.2}$
Width (σ_e) [keV] $\times 10^{-2}$	1.9 ± 0.3	$1.8^{+0.5}_{-0.3}$	$2.2^{+0.4}_{-0.3}$	$1.7^{+0.2}_{-0.3}$	$1.5^{+0.5}_{-0.3}$	$1.7^{+0.2}_{-0.3}$	$1.4^{+0.3}_{-0.2}$
Redshift (z_e) $\times 10^{-3}$	-0.0 ± 0.7	$-1.0^{+0.4}_{-0.3}$	$-0.0^{+0.6}_{-0.5}$	$0.0^{+0.6}_{-0.7}$	$2.6^{+0.6}_{-0.1}$	1.6 ± 0.8	$2.0^{+0.4}_{-0.9}$
Absorption lines							
Norm (N_a) $\times 10^{-3}$	$-0.5^{+0.5}_{-1.0}$	$-0.6^{+0.6}_{-0.8}$	-0.2 ± 0.2	$-0.4^{+0.3}_{-0.5}$	$-0.2^{+0.2}_{-0.9}$	$-0.4^{+0.3}_{-0.6}$	$-0.2^{+0.2}_{-0.6}$
Width (σ_a) [keV] $\times 10^{-2}$	$1.4^{+0.9}_{-0.6}$	$1.1^{+0.3}_{-0.4}$	$0.6^{+0.4}_{-0.2}$	0.7 ± 0.3	$1.6^{+1.4}_{-0.7}$	$0.9^{+0.5}_{-0.4}$	$1.6^{+1.1}_{-0.8}$
Redshift (z_a) $\times 10^{-3}$	$-0.9^{+0.9}_{-0.8}$	$-1.1^{+0.5}_{-0.6}$	-1.4 ± 0.3	-1.2 ± 0.3	$-0.8^{+0.8}_{-0.9}$	$-1.1^{+0.5}_{-0.4}$	$-0.8^{+0.8}_{-0.9}$
C-statistic / dof†	620 / 592	622 / 592	641 / 592	598 / 592	635 / 592	586 / 592	628 / 592

* Each orbital phase φ is shown as the median of the phase range from which each spectrum is extracted.
** The flux in $6.0 - 8.0\,\mathrm{keV}$.
† These values were calculated from the medians of the model predictions.

Table 3: Median and 90% interval of inferred parameters obtained by the analysis assuming a circular orbit(subsection 3.2).

Parameter \ Phase*	$\varphi = 0.0625$	$\varphi = 0.1875$	$\varphi = 0.4375$	$\varphi = 0.5625$	$\varphi = 0.6875$	$\varphi = 0.8125$	$\varphi = 0.9375$
Continuum							
Flux ($10^{-9}\,\mathrm{erg\,cm^{-2}\,s^{-1}}$)**	$1.17^{+0.02}_{-0.03}$	1.19 ± 0.02	1.17 ± 0.02	$1.20^{+0.03}_{-0.02}$	1.12 ± 0.04	1.07 ± 0.02	0.94 ± 0.03
Photon index (α)	$2.73^{+0.08}_{-0.09}$	2.73 ± 0.08	2.73 ± 0.08	$2.72^{+0.08}_{-0.09}$	2.75 ± 0.08	2.77 ± 0.08	$2.83^{+0.08}_{-0.09}$
Emission lines							
Norm (N_e) $\times 10^{-3}$	$1.2^{+1.5}_{-0.5}$	$1.2^{+1.8}_{-0.7}$	$0.8^{+0.4}_{-0.2}$	0.9 ± 0.2	$1.7^{+0.9}_{-0.6}$	$1.4^{+0.5}_{-0.4}$	$2.1^{+1.6}_{-0.9}$
Width (σ_e) [keV] $\times 10^{-2}$	1.9 ± 0.4	$1.8^{+0.5}_{-0.4}$	$2.1^{+0.3}_{-0.4}$	1.7 ± 0.2	1.8 ± 0.3	1.7 ± 0.3	$1.6^{+0.3}_{-0.2}$
Velocity amp. (v) [$\mathrm{km\,s^{-1}}$]				430^{+150}_{-140}			
Velocity offset (v_0) [$\mathrm{km\,s^{-1}}$]				100^{+93}_{-110}			
Phase offset (φ_0)				$-0.02^{+0.05}_{-0.04}$			
Absorption lines							
Norm (N_a) $\times 10^{-3}$	$-0.4^{+0.4}_{-0.2}$	$-0.7^{+0.7}_{-1.8}$	$-0.3^{+0.2}_{-0.5}$	$-0.3^{+0.1}_{-0.2}$	$-0.7^{+0.5}_{-0.8}$	$-0.3^{+0.3}_{-0.5}$	$-1.0^{+0.8}_{-1.6}$
Width (σ_a) [keV] $\times 10^{-2}$	$1.4^{+1.0}_{-0.7}$	1.2 ± 0.4	$0.7^{+0.5}_{-0.3}$	0.6 ± 0.2	1.4 ± 0.4	$0.9^{+0.4}_{-0.5}$	1.4 ± 0.3
Redshift (z_a) $\times 10^{-3}$	$-1.0^{+1.0}_{-1.4}$	-1.0 ± 0.5	-1.4 ± 0.3	-1.2 ± 0.2	$-0.6^{+0.6}_{-0.7}$	$-1.1^{+0.6}_{-0.5}$	$-0.6^{+0.6}_{-0.7}$
C-statistic / dof†				4318 / 4148			

* Each orbital phase φ is shown as the median of the phase range from which each spectrum is extracted.
** The flux in $6.0 - 8.0\,\mathrm{keV}$.
† This value was calculated from the median of the model predictions.